

Nonmonotonic magnetic field dependence of remanent ferroelectric polarization in reduced-graphene-oxide-BiFeO₃ nanocomposite

Tania Chatterjee,¹ Arnab Mukherjee,² Prabir Pal,³ S.D. Kaushik,⁴ V. Siruguri,⁴ Swarupananda Bhattacharjee,⁵ Chandan Kumar Ghosh,⁵ and Dipten Bhattacharya^{1,*}

¹*Advanced Materials and Chemical Characterization Division,
CSIR-Central Glass and Ceramic Research Institute, Kolkata 700032, India*

²*Functional Materials and Device Division, CSIR-Central Glass and Ceramic Research Institute, Kolkata 700032, India*

³*Energy Materials and Device Division, CSIR-Central Glass and Ceramic Research Institute, Kolkata 700032, India*

⁴*UGC-DAE Consortium for Scientific Research, Bhabha Atomic Research Centre, Mumbai 400085, India*

⁵*School of Materials Science and Nanotechnology, Jadavpur University, Kolkata 700032, India*

(Dated: October 14, 2021)

In a nanocomposite of reduced graphene oxide (RGO) and BiFeO₃ (BFO), the remanent ferroelectric polarization is found to follow nonmonotonic magnetic field dependence at room temperature as the applied magnetic field is swept across 0-20 kOe on a pristine sample. The remanent ferroelectric polarization is determined both from direct electrical measurements on an assembly of nanoparticles and powder neutron diffraction patterns recorded under 0-20 kOe field. The nanosized (~20 nm) particles of BFO are anchored onto the graphene sheets of RGO via Fe-C bonds with concomitant rise in covalency in the Fe-O bonds. The field-dependent competition between the positive and negative magnetoelectric coupling arising from magnetostriction due to, respectively, interface and bulk magnetization appears to be giving rise to the observed nonmonotonic field dependence of polarization. The emergence of Fe-C bonds and consequent change in the magnetic and electronic structure of the interface region has influenced the coupling between ferroelectric and magnetic properties remarkably and thus creates a new way of tuning the magnetoelectric properties via reconstruction of interfaces in nanocomposites or heterostructures of graphene/single-phase-multiferroic systems.

PACS numbers: 75.80.+q, 75.75.+a, 77.80.-e

I. INTRODUCTION

The reconstruction of crystallographic, magnetic, and electronic structures at the interface turns out to be quite an effective way of preserving the multiferroic orders and augmenting the coupling among the order parameters in multiferroics based heterostructures/composites [1]. Among different heterostructures or composites, graphene/BiFeO₃ or reduced-graphene-oxide-BiFeO₃ systems have attracted a lot of attention [2–6]. Large exchange field B_{ex} (of the order of ten to hundred tesla) in graphene/BiFeO₃ heterostructure induces proximity effect driven magnetism [3, 5] while, in graphene/BaMnO₃ system, the magnetic structure of BaMnO₃ exhibits change from antiferromagnetic to ferromagnetic orientation at the interface [4]. It has also been shown [7] that graphene-methylammonium lead iodide (CH₃NH₃PbI₃) composite exhibits ferroelectricity because of reconstruction of crystallographic structure in the interface regions. Given all these results, it is important to examine how reconstruction of magnetic and electronic structures by exchange coupled surface atoms of graphene and nanoscale BiFeO₃ influences the multiferroicity in BiFeO₃. In this paper, we show that the reduced-graphene-oxide-BiFeO₃ (RGO/BFO) nanocomposite exhibits significant decrease in ferromagnetic com-

ponent yet enhancement in coercivity and remarkable nonmonotonic variation of ferroelectric polarization with applied magnetic field (H). Bulk BiFeO₃ exhibits [8] suppression of off-centering of Fe ions [and consequently, suppression of ferroelectric polarization (P)] below T_N (off-centering of Bi ions remains unaffected) since it is driven by negative magnetostriction within Fe-O-Fe spin structure. It also yields monotonic suppression of P under H . The P arising out of magnetostriction due to the magnetization in the interface region of the RGO/BFO nanocomposite, on the other hand, could exhibit monotonic rise with H . Field-dependent competition between these two opposite trends (emerging within bulk and interface spin structures) possibly yields this nonmonotonic H dependence of P in the nanocomposite.

II. EXPERIMENTAL DETAILS

The RGO/BFO nanocomposite has been prepared by hydrothermal technique. Graphene oxide (GO) was prepared from graphite via modified Hummers method [9] in which 70 ml of sulphuric acid (H₂SO₄) was taken within an ice bath (for maintaining the temperature below 20°C) and 1g of graphite powder and 0.5g of sodium nitrate (NaNO₃) were added to the acid solvent and stirred for a while. After that, 3g of potassium permanganate (KMnO₄) was added gradually and stirred vigorously. We allowed the bath temperature to stabilize and then removed the ice bath to attain room temperature.

*Electronic address: dipten@cgcric.res.in

The mixed solution was stabilized at room temperature for 2h and then diluted by adding 5% hydrogen peroxide (H_2O_2) solution slowly till the color turned brownish yellow. It confirmed complete oxidation of graphite. Finally, the solution was stirred for 30 minutes to further exfoliate the as-formed graphite oxide (GO). The GO, thus synthesized, was collected by filtration and washing for several times with 1N hydrochloric acid (HCl) and deionized water. Synthesized GO and BFO precursors - $[\text{Bi}(\text{NO}_3)_3 \cdot 5\text{H}_2\text{O}]$ and $[\text{Fe}(\text{NO}_3)_3 \cdot 6\text{H}_2\text{O}]$ - were used for the hydrothermal synthesis [10] of the composite. The aqueous solution of GO was reduced to form reduced graphene oxide (RGO) using ascorbic acid as the reducing agent. The 8M potassium hydroxide (KOH) and the precursors of BFO were added in stoichiometric ratio. Once homogenized, the as-prepared RGO solution was added to the mixture to maintain 1.50 weight% of RGO in the resulting mixture. The ammonium hydroxide (NH_4OH) was added in 1.0 weight% to facilitate the formation of BiFeO_3 nanoparticles embedded in the RGO matrix. The solution was stirred for 30 minutes and put into an autoclave for hydrothermal treatment at 170°C for 2, 4, 5, 6 hours. The sample treated hydrothermally for 6h turned out to be phase pure and was designated as Com-H. The nanocomposite Com-H was further heated to 550°C for 20 minutes. This treatment removes the carbon skeleton and leaves the bare nanoparticles of BiFeO_3 (BFO-H). The thermogravimetric analysis was carried out under both air and inert (Ar) atmosphere to track the formation of BFO-H.

All the samples were characterized by powder X-ray diffraction (XRD), infrared (IR) and Raman spectroscopy, scanning and tunneling electron microscopy (SEM and TEM), and x-ray photoelectron spectroscopy (XPS). The XPS measurements were performed by PHI 5000 VERSAPROBE II, Physical Electronics System, equipped with monochromatic Al k_α (1486.7 eV) focussed x-ray source and a multi-channel hemispherical electron energy analyzer. All the spectra were collected at an emission angle of 45° with the base vacuum of 5.0×10^{-10} mbar. The binding energies were referenced by measuring C 1s and keeping it at 284.6 eV. The total energy resolution was estimated to be ~ 400 meV for monochromatic Al k_α line with pass energy 11.750 eV. A charge neutralizer was used to compensate the surface charging of the samples. A background has been subtracted from the measured raw data. The magnetic hysteresis loops were measured by LakeShore Vibrating Sample Magnetometer (VSM; Model 7407) under ± 20 kOe field at room temperature while the ferroelectric polarization was measured by the Precision LC-II (Radiant Technologies Inc.) ferroelectric loop tester. For preparing the samples for electrical measurements, nanoparticles were dispersed within ethanol and spin coated onto the Si/SiO₂ substrate to form the films [11] (thickness of the film was ~ 10 nm as measured by ellipsometry). Silver dots were used as electrodes. The powder neutron diffraction patterns were recorded at room temperature

at the PD-3 beamline of National Facility for Neutron Beam Research (NFNBR), Dhruva Reactor, Mumbai using a monochromatic beam of wavelength 2.315 Å. The magnetic field was varied across 0-20 kOe.

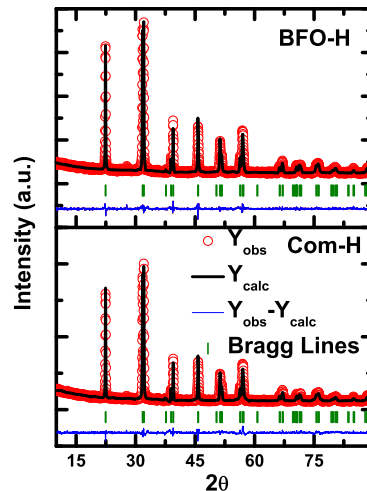


FIG. 1: The room temperature x-ray diffraction data and their refinement.

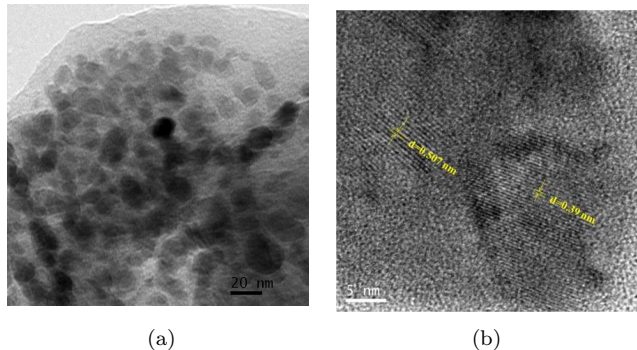
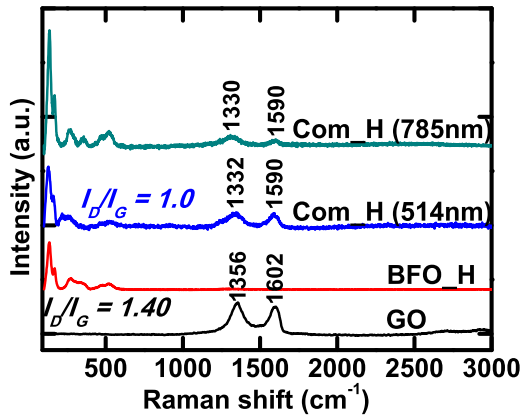


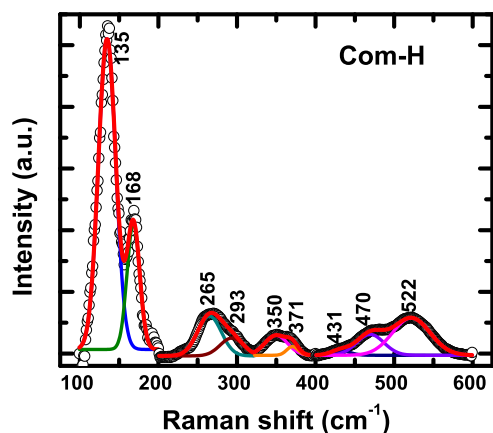
FIG. 2: The (a) bright field TEM and (b) high resolution TEM (HRTEM) images of the BFO/RGO nanocomposite.

III. RESULTS AND DISCUSSION

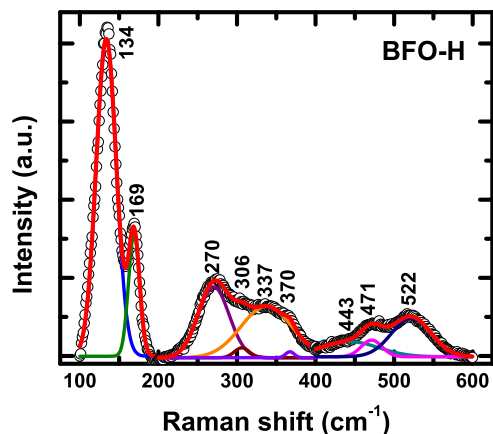
Figure 1 shows the XRD data for Com-H and BFO-H. The data were refined by FullProf. Both Com-H and BFO-H were found to assume $R3c$ space group. The average global crystallographic structure has not changed in the nanocomposite. BiFeO_3 assumes $R3c$ symmetry due to the presence of both polar distortion as well as antiferrodistortive rotation of FeO_6 octahedra (which was shown [12] to be related to the magnetization) around the axis of polarization [111]. The detailed results of the refinement (lattice parameters, ion positions, bond lengths



(a)



(b)



(c)

FIG. 3: Raman spectra for the composite (COM-H), pure BFO (BFO-H), and GO systems.

and angles) including the fit statistics are given in the

supplementary document [11]. Figures 2(a),(b) show the bright field TEM and high resolution TEM (HRTEM) images for Com-H. The image analysis yields the average size of BFO particles to be ~ 18 - 20 nm which is comparable to the particle size of BFO-H (shown in [11]). A certain fraction of the BFO particles are anchored onto the RGO layers. The HRTEM image shows the interface between (012) plane of BFO ($d = 0.39$ nm) particle and the RGO layer with interlayer spacing 0.49 nm. It indicates deposition of graphene layer onto the (100)_c plane of BiFeO₃. The interlayer spacing of RGO is much larger than that in graphite ($d = 0.37$ nm) due to exfoliation.

The Raman spectrometry of the Com-H and BFO-H are shown in Figs. 3(a),(b),(c). The experiments were carried out with both 514 nm and 785 nm He-Ne laser excitations. The 514 nm laser probes the organic compound while the inorganic system is probed by 785 nm laser. It is found that the intensity ratio of the characteristic D and G peaks at 1355 cm^{-1} and 1593 cm^{-1} - which, respectively, correspond to the dangling bonds from defects containing sp^3 hybridized orbitals and planar vibration of C ions bonded via sp^2 hybridized orbitals - is 1.00 in the Com-H. Using the relations [13, 14] $L_D^2 = [(1.8 \pm 0.5) \times 10^{-9} \times \lambda^4] / [I_D/I_G]$ and $n_D = 10^{14} / \pi L_D^2$, where L_D is the effective distance between the defects (in nm), n_D is the defect concentration (in cm^{-2}), λ is the wavelength of the excitation, and I is the intensity of the D or G peaks, we find that the defect concentration (n_D) and the spacing between the defects (L_D) in the RGO layers are $1.98 \times 10^{27} \text{ cm}^{-2}$ and 12.67 nm, respectively. The corresponding figures for the graphite oxide (GO) are $2.77 \times 10^{27} \text{ cm}^{-2}$ and 10.70 nm, respectively. The decrease in defect concentration and increase in defect spacing in Com-H with respect to GO indicates lesser extent of functionalization of the graphene layer in Com-H. This observation could have some significance in pointing out that the BiFeO₃ nanoparticles used for functionalization of the graphene results in co-existence of both bonded and nonbonded nanoparticles.

The characteristic modes of BFO exhibits substantial red and blue shifts in the Com-H. According to group theory, there are 13 Raman active modes of BFO with the rhombohedral $R3c$ structure which are defined by the following irreducible representations [15] $\Gamma_{Raman, R3c} = 4A_1 \oplus 9E$; where 4 A_1 modes are polarized along z axis and the rest 9 E doubly degenerate modes are polarized along x - y plane. In BFO-H and Com-H (Figs. 3b and 3c), nine active modes could be observed out of the 13 modes. The lineshape of the peaks was fitted by Gaussian function. Their assignment [15, 16] together with the modes calculated from first-principles [15] are listed in Table I.

The lower order A_1 and E modes are related to the Bi-O and Fe-O vibration while the higher order peaks arise due to the change in the oxygen motion states. Comparison of the Raman spectra observed in BFO-H and Com-H (Fig. 3) reveals that (i) the lower order modes (till 167 cm^{-1}), influenced by Bi atoms, do not exhibit

TABLE I: The Raman modes for Com-H and BFO-H samples.

Raman modes	BFO-H (cm^{-1})	Com-H (cm^{-1})	Calculated (cm^{-1})
$E(\text{TO})$	133.5	134.2	152
$A_1(\text{TO})$	169.3	168.7	167
$A_1(\text{LO})$	270.3	265.4	277
$A_1(\text{TO})$			266
$A_1(\text{TO})$	306.2	293.1	318
$E(\text{LO})$	337.5	350.7	332
$E(\text{TO})$			335
$E(\text{TO})$	369.7	371.1	378
$E(\text{LO})$			386
$E(\text{TO})$	443.4	431.2	409
$E(\text{LO})$			436
$A_1(\text{LO})$	471.2	470.1	509
$A_1(\text{TO})$	522.1	522.4	517

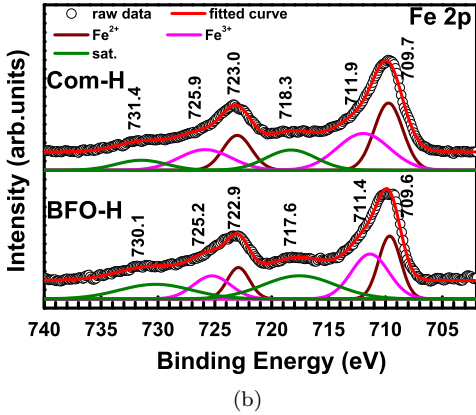
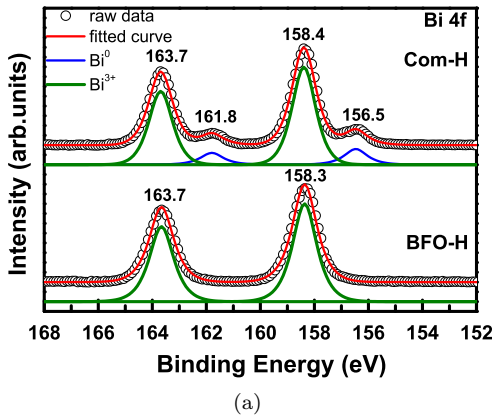


FIG. 4: X-ray photoelectron spectra and their fitting for (a) Bi 4f and (b) Fe 2p in pure BFO (BFO-H) and composite (COM-H) systems.

any substantial shift while (ii) the modes influenced by Fe ions and oxygen motion states are either red or blue shifted. For example, the $A_1(\text{LO})/A_1(\text{TO})$ and $E(\text{TO})$ modes at $\sim 270 \text{ cm}^{-1}$, $\sim 306 \text{ cm}^{-1}$, and $\sim 443 \text{ cm}^{-1}$ are

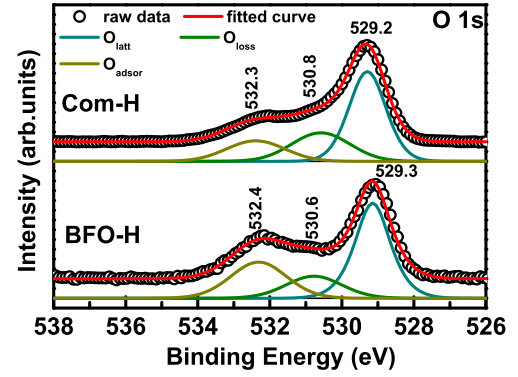


FIG. 5: X-ray photoelectron spectra and their fitting for C 1s in pure BFO (BFO-H) and composite (COM-H) systems.

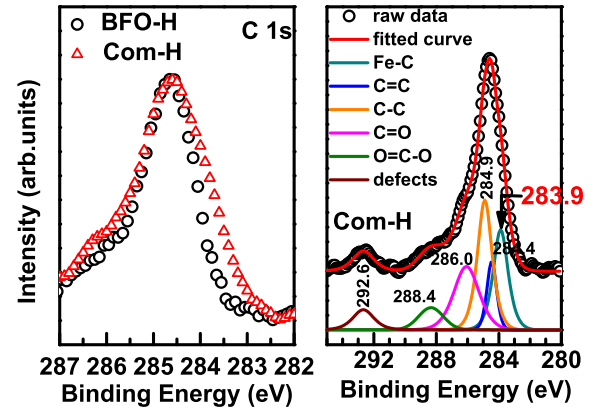


FIG. 6: X-ray photoelectron spectra and their fitting for O 1s in pure BFO (BFO-H) and composite (COM-H) systems.

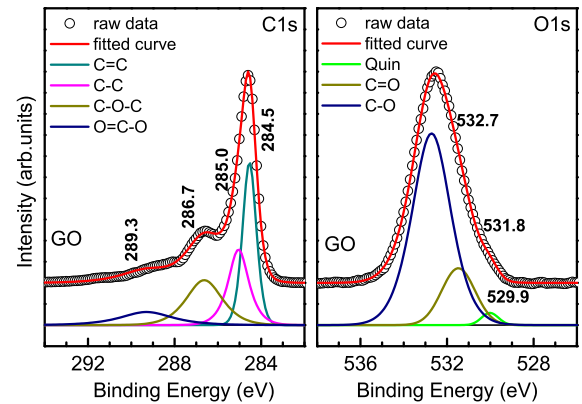


FIG. 7: High resolution C 1s and O 1s X-ray photoelectron spectra of GO highlighting presence of different species on its surface.

redshifted by $5\text{-}13\text{ cm}^{-1}$ while the $E(LO)/E(TO)$ one at $\sim 337.5\text{ cm}^{-1}$ is blueshifted by $\sim 13\text{ cm}^{-1}$ in Com-H. This could be due to the change in the Fe-O bond lengths and the motion states of oxygen. The formation of Fe-C bonds at the BFO/RGO interface (discussed later) could have some influence on the bulk lattice and its distortion. The distortion in the Fe-O bonds have contributions from both polar distortion and antiferrodistortive tilt. The calculation of the Fe-O bond length (supplementary data[11]) shows that indeed the difference in the bond lengths has decreased in Com-H. Similar observation has earlier been made by others [17] in different perovskite oxide systems. The infrared spectra too corroborate these observations together with the confirmation of formation of RGO and are included in the supplementary document [11].

The high resolution XPS data for Bi 4f and Fe 2p are shown in Figs. 4(a) and 4(b), respectively. The Bi $4f_{7/2}$ and $4f_{5/2}$ spin-orbit doublet peaks are located at 158.4 and 163.7 eV, respectively, which are found to correspond to Bi^{3+} states from Bi-O bonds. Interestingly, the binding energy of Bi^{3+} states remains same in both the BFO-H and Com-H samples. It indicates that no substitution has taken place at the Bi^{3+} sites in the Com-H sample. Of course, an additional weak pair of doublet peaks was observed in Com-H in the lower binding energy side which points to the presence of Bi^0 states. To estimate the percentage of Bi^0 states in the Com-H sample, we have adopted the χ^2 iterative fit of the Bi 4f core-level region using two pair of doublet components corresponding to the Bi^{3+} (grey) and Bi^0 (blue) states, as shown in Fig. 4(a). Except for the peak area, the energy positions, line shapes, widths, and all other parameters were kept same during the fitting of two pairs of doublet peaks. The Bi^0 states $4f_{7/2}$ and $4f_{5/2}$ (spin-orbit doublet peaks) are centered at ~ 156.5 and ~ 161.8 eV, respectively. The relative percentage of Bi^0 states is found to be $\sim 14.3\%$.

The $\text{Fe}2p_{3/2}$ and $\text{Fe}2p_{1/2}$ spin-orbit doublet peaks are located around 709.6 eV and 722.9 eV, respectively, with a pair of shake-up satellite peaks [18] located at 8.0 eV above their spin-orbit doublet peaks. We have carefully fitted the spectra using the following fitting parameters for the Fe^{2+} : spin-orbit splitting 13.3 eV, branching ratio 2.0, full widths at half maximum (FWHM) 2.3 eV; an integral background was subtracted before fitting. Similarly, the spectra for Fe^{3+} were fitted by considering spin-orbit splitting 13.8 eV, branching ratio 2.0, and FWHM 3.8 eV. The fitted Fe 2p spectra highlight the characteristic doublet peaks of Fe^{2+} -O species at ~ 709.6 eV and ~ 722.9 eV for $\text{Fe}2p_{3/2}$ and $\text{Fe}2p_{1/2}$, respectively, and the doublet peaks of Fe^{3+} -O species at ~ 711.4 eV and ~ 725.2 eV for $\text{Fe}2p_{3/2}$ and $\text{Fe}2p_{1/2}$, respectively. It is to be noted that the composite sample shows no change in the peak positions, except for the Fe^{3+} oxidation state which shows a shift of ~ 0.6 eV toward higher binding energy. This chemical shift of Fe^{3+} arises due to the variation in the electronegativity of Fe and O in the composite sample. The $\text{Fe}^{2+}:\text{Fe}^{3+}$ ratio turns out to be 45.4:54.6 and

49.4:50.6 in BFO-H and Com-H, respectively.

Figure 5 shows the C 1s core-level spectra for both BFO-H and Com-H. The spectra corresponding to Com-H were fitted by using the contribution of the following six components: (i) defects, (ii) O=C-O, (iii) C=O, (iv) C-C, (v) C=C, and (vi) Fe-C bonds. The peak at 283.9 eV corresponds to the Fe-C bonds. Existence of this peak proves the presence of Fe-C bonds in the Com-H sample. Figure 6 shows the O 1s peak fitted with contribution from the lattice oxygen, oxygen loss, and surface oxygen. Their characteristic peaks appear at lower, intermediate, and higher binding energies. For both the samples, the O 1s peaks were fitted by keeping the peak position, line shape, and the width same. The oxygen loss turns out to be 18.1 and 26.5%, respectively, for the BFO-H and Com-H.

We analyzed the C 1s spectra for Com-H quantitatively for determining the concentration of different bonds such as Fe-C, C-C, C=C, O=C-O, O-C-O and compared the results with those obtained from the analysis of the spectra (Fig. 7) for pure GO. The comparison is given in the tabular form in Table II. The concentration of C=C bonds is found to have decreased in Com-H in comparison to that in GO because of the rise in the Fe-C bonds in Com-H. The difference between the concentration of C=C bonds alone in GO and that of C=C and Fe-C bonds ($\sim 3\%$) in Com-H is accounted for in the rise in C-C bonds in Com-H. Expectedly, the concentration of O=C-O and O-C-O bonds has decreased in Com-H because of reduction of GO in the composite. Presence of C-C bonds also indicates that not all the surface carbon ions of graphene are bonded to the Fe ions of BiFeO_3 particles. Therefore, both bonded and nonbonded BiFeO_3 particles coexist in the Com-H sample. As discussed later, relative concentration of bonded BiFeO_3 particles plays an important role in governing the magnetoelectric properties of the nanocomposite.

TABLE II: The relative concentration (in %) of surface and interface bonds in GO and Com-H.

Bonds	GO (% bonds)	Com-H (% bonds)
Fe-C	-	22.69
C=C	35.90	9.67
C-C	26.19	29.04
O-C-O	26.37	23.65
O=C-O	11.54	8.20
Defects	-	6.74

Summarizing the results obtained from the X-ray diffraction, transmission electron microscopy, IR and Raman spectrometry, and X-ray photoelectron spectroscopy, we notice that (i) the functionalization of RGO by BFO nanoparticles of average size ~ 20 nm is incomplete as both bonded and nonbonded BFO nanoparticles coexist (defect spacing in RGO/BFO nanocomposite is higher than that in GO which is obtained from greater extent

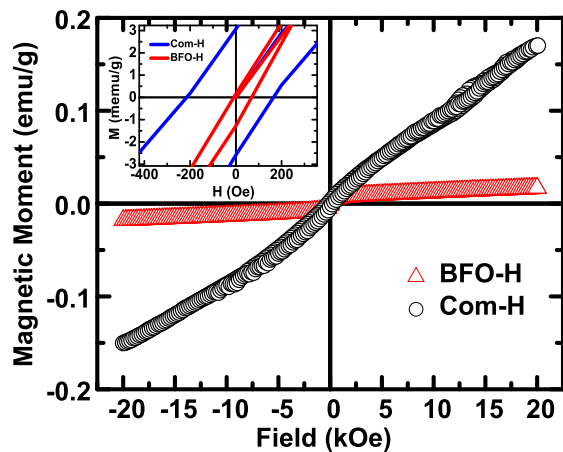


FIG. 8: The room temperature magnetic hysteresis loops for the samples; inset: the portion near the origin has been blown up.

of functionalization of graphene layers by oxygen), (ii) indeed Fe-C bonds have formed at the RGO/BFO interface in the cases where BFO nanoparticles are bonded with RGO in Com-H sample leading to the concomitant rise in covalency in Fe-O bonds, (iii) in spite of lattice distortion (resulting in red and blue shift of characteristic Raman modes), the average global crystallographic structure is still retaining $R3c$ symmetry.

Figure 8 shows the room temperature magnetization (M) versus field (H) hysteresis loops for Com-H and BFO-H. Contrary to the prediction made [4] in the case of graphene/BaMnO₃, the ferromagnetic component is found to have weakened in Com-H. The magnetization (M) does not tend to saturate ($M_{20kOe} = 0.017$ and 0.17 emu/g, respectively, for BFO-H and Com-H) within the applied field limit (± 20 kOe). The coercivity (H_C), of course, turns out to be much larger in Com-H ($H_C = 38$ and 190 Oe, respectively, for BFO-H and Com-H). It is well known now that, for BFO, the nanoparticles exhibit enhancement in ferromagnetic component because of larger spin canting and incomplete spin spiral (this is effective in particles smaller than ~ 62 nm - the wavelength of the spin spiral in BiFeO₃). It has been shown [19] from powder neutron diffraction experiment that the canting angle could enhance to $\sim 6^\circ$ (from $\sim 1^\circ$ in bulk sample [12]) in particles of size ~ 25 nm. In the present case, variation of the ferromagnetic component could result from change in the charge states of the ions and formation of Fe-C bonds at the RGO/BFO interface in Com-H. The Fe-C exchange coupling interaction (which leads to the exchange splitting of the Dirac bands in graphene layer as well as renormalization of the Fe moments in the interface; exchange field was shown [3, 5] to be of the order of 10 to 100T at the BiFeO₃/graphene interface) possibly gives rise to the renormalization of the exchange coupling parameters at the bulk as well which, in turn, could give rise to drop in the spin canting an-

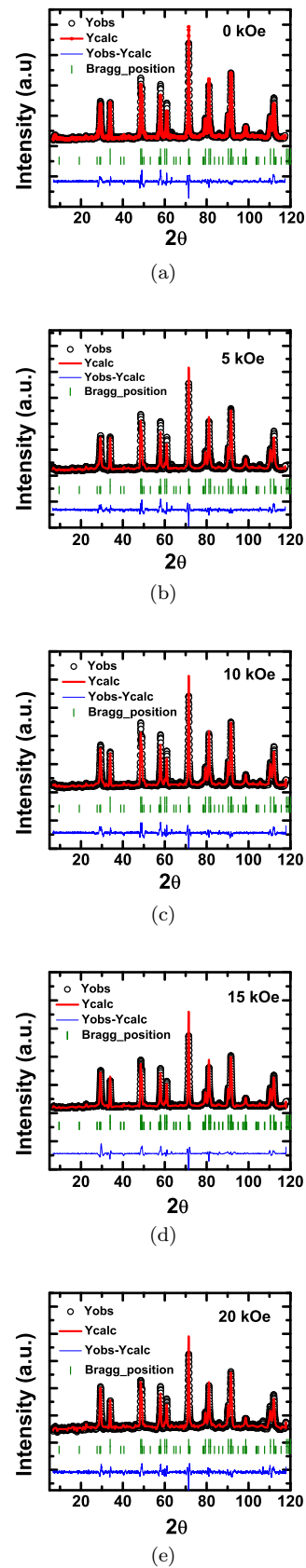


FIG. 9: Powder neutron diffraction data and their refinement by FullProf; $R3c$ and Γ_1 phases have been considered; the data were recorded at room temperature under different magnetic field.

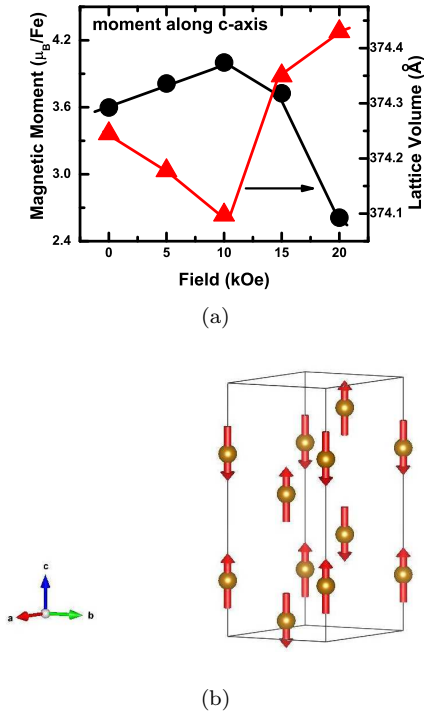


FIG. 10: (a) The variation of the lattice volume and magnetic moment along c-axis with field obtained from the refinement of neutron diffraction data; (b) the spin structure corresponding to Γ_1 irreducible representation.

gle. The ferromagnetic component, therefore, weakens. Interestingly, in spite of weakening of the ferromagnetic component, the coercivity (H_C) turns out to be larger in Com-H. The pinning of domains by defects appears to be stronger in Com-H. Because of the surface ferromagnetism and core antiferromagnetism, small amount of exchange bias field (H_E) could also be observed ($H_E = 31$ and -25 Oe, respectively, for BFO-H and Com-H).

The powder neutron diffraction data were recorded on Com-H sample at room temperature under different magnetic field across 0-20 kOe. We ignored the spin spiral and considered collinear structure. Long spiral length (~ 62 nm) in BiFeO_3 allows such consideration. The data were refined by FullProf by considering the $R3c$ space group and Γ_1 irreducible representation (propagation vector $k = 0$). Group theory analysis of the spin structure for $R3c$ and propagation vector $k = 0$ yields three irreducible representations Γ_1 , Γ_2 , and Γ_3 (reducible representation $\Gamma(\text{Fe}, 6a) = \Gamma_1 + \Gamma_2 + 2\Gamma_3$). Refinement shows that the Γ_1 offers the best fitting [11]. The refinement is shown in Fig. 9. Because of the limitations of the current neutron diffraction experiments, we could not detect the change in spin structure in the RGO/BFO nanocomposite with respect to the spin structure of nanoscale BiFeO_3 . The lattice parameters, magnetic moment, ion positions, and the fit statistics are

included in the supplementary document [11]. The variation of the magnetic moment along c-axis (c_3) with the applied magnetic field together with the collinear spin structure corresponding to Γ_1 are shown in Fig. 10. The nonmonotonic field dependence of c_3 possibly reflects field-dependent competition between interface and bulk magnetization and consequent renormalization of the average bulk magnetic moment calculated from the powder neutron diffraction by considering collinear G-type spin structure Γ_1 . Interestingly, the lattice volume is found to decrease and then increase (Fig. 10) indicating switch from negative to positive magnetostriction as the applied magnetic field is enhanced across 0-20 kOe. This could be (as discussed later) due to field-dependent competition between bulk and surface/interface magnetic anisotropy.

We finally discuss the results of the measurement of ferroelectric polarization under different magnetic fields. Both the positive-up-negative-down (PUND) [20] and remanent ferroelectric hysteresis loop protocols [21] were employed for the measurements. Figure 11 shows the results for Com-H. Under zero magnetic field, the polarization (P_R) turns out to be ~ 4.0 nC/cm² [11]. Along with the results obtained from direct electrical measurements on the nanoparticle assembly, the net off-centered displacement (δ) in the unit cell, estimated from the powder neutron diffraction data, are also plotted in Fig. 11. Interestingly, both the P_R and δ exhibit nonmonotonic pattern of variation with the magnetic field (H) across 0-20 kOe. *This is the central result of this paper.* There is, however, quantitative difference between the $P_R - H$ patterns obtained from direct electrical measurements by PUND and remanent hysteresis protocols. As pointed out in a detailed work [21], PUND protocol contains contribution from nonhysteretic polarization as well. As a result, the intrinsic hysteretic polarization component cannot be accurately extracted by PUND protocol. The close conformation of the $P_R - H$ and $\delta - H$ patterns obtained from remanent hysteresis protocol and neutron diffraction data provides further proof of better efficacy of remanent hysteresis protocol in extracting the intrinsic hysteretic polarization in a sample where contribution from several spurious effects obscures the intrinsic effect. Nonmonotonic nature of $P_R - H$ in RGO/BFO nanocomposite, therefore, is intrinsic. Pristine BiFeO_3 , on the contrary, exhibits monotonic suppression of P_R with the increase in magnetic field because of negative magnetoelectric coupling [8]. In BiFeO_3 , stabilization of $R3c$ structure yields coupling of polarization and magnetization via coupling between polar distortion and antiferrodistortion of FeO_6 octahedra. While polar distortion takes place along [111] (along [001] in hexagonal setting), antiferrodistortive rotation of FeO_6 octahedra occurs around [111]. This, in turn, is coupled to the magnetization contained in the (111) plane. Symmetry bars the 180° switching of the sense of antiferrodistortive rotation of FeO_6 octahedra (and hence the magnetization) as a result of 180° switching of polar distortion in a single step [12]. However, it has been demonstrated [22] that

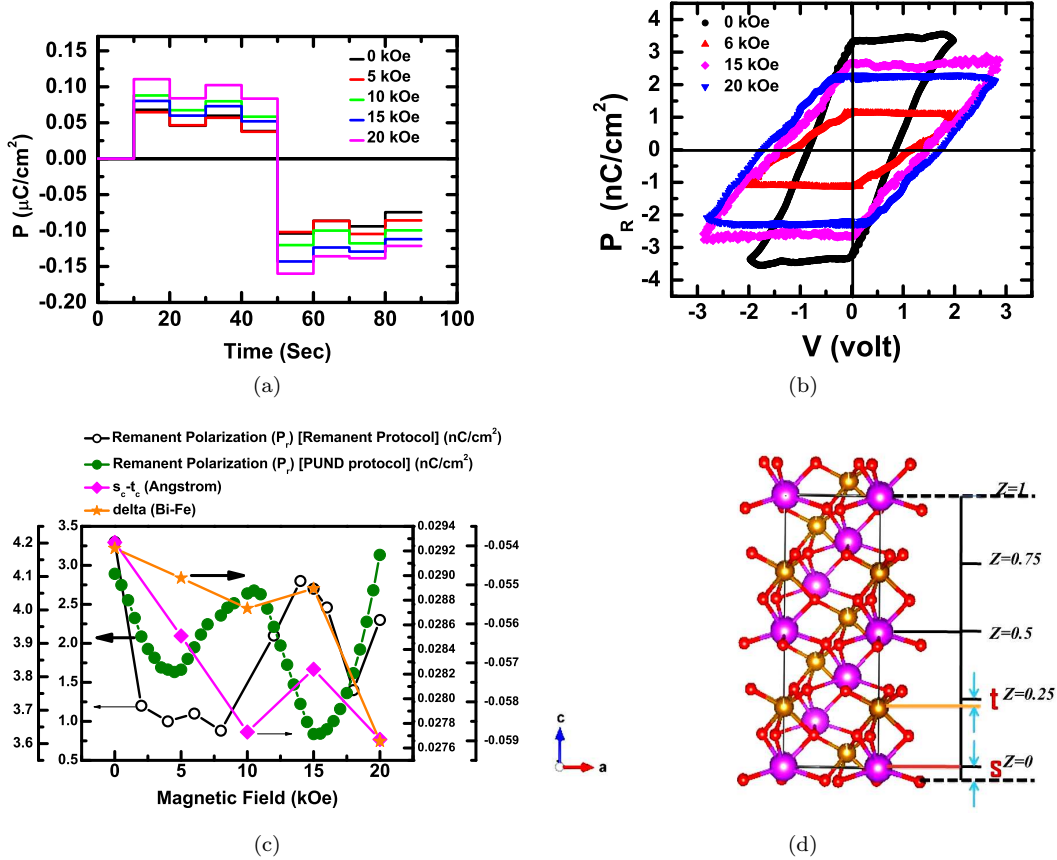


FIG. 11: The remanent ferroelectric polarization under different magnetic fields obtained from the (a) PUND protocol, (b) remanent hysteresis loops; (c) variation of P_R with H obtained from remanent hysteresis loops (inner left axis) and PUND (outer left axis); unit cell off-centered displacement - s_c-t_c (inner right axis) and net off-centering with respect to the oxygen cages (outer right axis) - obtained from refinement of powder neutron diffraction data; (d) section of the $R3c$ crystallographic structure is shown in hexagonal setting to highlight the off-centered displacements of Bi and Fe ions along $[001]$.

indeed the deterministic 180° switching of magnetic domains takes place (as a result of that of the ferroelectric domains) under electric field in two steps - first, in-plane rotation by 71° and then out-of-plane rotation by 109° . Piezo- and magnetostriction associated with this complex pathway of domain rotation influences the magnitude of the polarization and magnetization of the domains.

As the magnetic field is swept from zero to a maximum, negative magnetoelectric coupling (arises from influence of negative magnetostriction on piezoelectricity) in pure BiFeO_3 yields decrease in polarization with increase in magnetization [8]. Suppression of polarization under magnetic field was observed not just in bulk form of the sample but in nanoscale samples as well [23]. The bulk and surface magnetocrystalline anisotropy (K_B and K_S) results in negative bulk and surface magnetostriction (λ_B and λ_S) in nanoscale BiFeO_3 assuming $R3c$ structure. Negative magnetostriction leads to negative magnetoelectric coupling, i.e., suppression of polarization under magnetic field. In an assembly of sin-

gle crystalline nanoparticles, averaging over the domain configurations and the properties, therefore, yields similar decrease (increase) in polarization (magnetization) at any given state. This magnetostrictive suppression of piezoelectricity, observed in pure BiFeO_3 , can be altered and consequent enhancement of magnetostriction driven polarization is possible. In $\text{BiFeO}_3/\text{reduced-graphene-oxide}$ nanocomposite, emergence of Fe-C bonds (from strong hybridization of $3d_{x^2-y^2}/3d_{z^2}$ orbitals of Fe and p_z orbitals of C) and consequent magnetization at the graphene- BiFeO_3 interface regions opens up this possibility. It has already been shown [5, 24] that the Fe-C bonding leads to the generation of large exchange field (of the order of 10 to 100T) which gives rise to the split of Dirac bands in the graphene layer as well as proximity induced magnetization. This exchange field alters the magnetization at the interface reflected in the enhancement of the antiferromagnetic component in RGO/BFO nanocomposite. Change in the magnetic moment at the interface was earlier predicted by theoretical calculations

[25]. The anisotropy (K_I) associated with this interface magnetization could yield positive surface magnetostriction. This, in turn, could give rise to the rise in P_R with H , i.e., positive magnetoelectric coupling. It has been shown [26] earlier that indeed the ratio of surface/interface anisotropy and bulk anisotropy (K_I/K_B) governs the spin structure significantly. Different structure emerges as K_I or K_S enhances with respect to K_B . Conversely, different spin structures at the interface could yield different K_I and, as a consequence, positive interface magnetostriction. Field-dependent switch from negative to positive magnetostriction has indeed been observed in the present case. The mapping of lattice volume with the applied magnetic field (Fig. 10) shows decrease and then increase in lattice volume as the field is swept across 0-20 kOe. This observation underlines the important role of interface magnetization driven by Fe-C bonds. Of course, how K_I , in the present case, yields positive interface magnetostriction and the ratio K_I/K_B governs the influence of magnetostriction on piezoelectricity as a function of applied magnetic field (H) - from negative to positive - needs to be studied in detail separately.

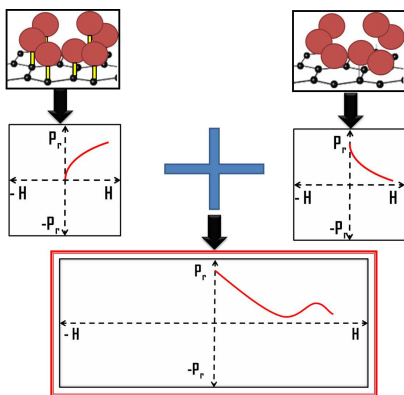


FIG. 12: The schematic of the bonded and nonbonded BiFeO_3 particles with reduced graphene oxide layers; the bonded particles because of the presence of Fe-C bonds and exchange coupling interactions across them could offer positive magnetostrictive magnetoelectric coupling; the nonbonded ones, on the other hand, would exhibit negative magnetoelectric coupling; field-dependent competition between these two fractions is eventually yielding the nonmonotonic variation of P_R with H . Tuning of the volume fractions of the bonded and nonbonded BiFeO_3 particles, therefore, offer a pathway to tune the switching of magnetoelectric coupling - from purely negative to mixed positive and negative to purely positive.

Based on the above discussion, in Fig. 12, we present the schematic of the model which describes the physics behind the observed nonmonotonic $P_R - H$ pattern. The Com-H sample contains both bonded (via Fe-C bonds) and nonbonded (attached via van der Waals bonds)

BiFeO_3 particles. While magnetostriction due to symmetric exchange interaction (i.e. the exchange interaction which does not involve spin-orbit coupling) across Fe-O-Fe bonds, in the absence (relevant for BFO-H) and presence of proximity coupling via formation of Fe-C bonds (relevant for Com-H because of the presence of these bonds at the interface regions), yields, respectively, negative and positive magnetoelectric coupling, the field-dependent competition (shown in Fig. 12) between the positive and negative magnetoelectric coupling in bonded and nonbonded BiFeO_3 particles yields the observed nonmonotonic pattern of variation of P_R with H . The P_R decreases initially and then rises and finally decreases again as the applied magnetic field is swept from zero to ~ 20 kOe. Relative volume fraction of the bonded and nonbonded BiFeO_3 nanoparticles governs the relative strength of increase and decrease of the P_R as a function of H . Coexistence of positive and negative magnetostrictive regions and engineering of their respective volume fractions have earlier been demonstrated [27] within the bulk of the Fe-Ga alloys. This was projected to yield field-dependent switch in ferroelectric polarization in ferroelectric/Fe-Ga alloy multilayer composites. In the present case, reconstruction of interface in reduced-graphene-oxide/ BiFeO_3 nanocomposite is shown to be actually yielding the result projected in Ref. 27. Engineering of the bulk and interface anisotropies and hence of the bulk and interface magnetostrictions further could yield eventually an interesting custom-designed periodic nonmonotonic pattern of variation of P_R with H . Such custom-designed $P_R - H$ pattern will obviously expand the horizon of the nanospintronic applications by a great extent.

IV. CONCLUSION

In conclusion, the RGO/BFO nanocomposite exhibits a range of interesting properties such as decrease in ferromagnetic component yet rise in coercivity and finite negative exchange bias and nonmonotonic dependence of ferroelectric polarization on applied magnetic field. This ensemble of unusual properties results from reconstruction of BiFeO_3 /graphene interface via formation of Fe-C bonds and could find interesting applications. It could also trigger fresh research on atomic scale engineering of the interfaces in the composites or heterostructures for far enhanced functionalities.

ACKNOWLEDGMENTS

One of the authors (T.C.) acknowledges DST-INSPIRE research fellowship. Another author (A.M.) acknowledges support from Science and Engineering Research Board (SERB), Government of India (Grant No. CRG/2021/002132).

-
- [1] See, e.g., W. Huang *et al.*, *Appl. Phys. Rev.* **5**, 041110 (2018).
- [2] Z. Zanolli, *Sci. Rep.* **6**, 31346 (2016).
- [3] H-D Song *et al.*, *Nano Lett.* **18**, 2435 (2018).
- [4] Z. Zanolli *et al.*, *Phys. Rev. B* **98**, 155404 (2018).
- [5] Y-F Wu *et al.*, *Phys. Rev. B* **95**, 195426 (2017).
- [6] A.K. Chaurasiya *et al.*, *Phys. Rev. B* **99**, 035402 (2019).
- [7] G. Volonakis *et al.*, *J. Phys. Chem. Lett.* **6**, 2496 (2015).
- [8] S. Lee *et al.*, *Phys. Rev. B* **88**, 060103(R) (2013).
- [9] W.S. Hummers *et al.*, *J. Am. Chem. Soc.* **80**, 1339 (1958).
- [10] T. Li *et al.*, *Mater. Lett.* **91**, 42 (2013).
- [11] The supplementary document contains XRD and neutron data fit statistics, details of crystallographic structure, IR spectrometry, TEM and FESEM images, and results of polarization measurements. It is available from the author on request.
- [12] C. Ederer and N.A. Spaldin, *Phys. Rev. B* **71**, 060401(R) (2005).
- [13] E.H. Martins Ferreira *et al.*, *Phys. Rev. B* **82**, 125429 (2010).
- [14] A.Y. Sheng Eng *et al.*, *ACS Nano* **7**, 5930 (2013).
- [15] P. Hermet *et al.*, *Phys. Rev. B* **75**, 220102(R) (2007).
- [16] R. Palai *et al.*, *Phys. Rev. B* **81**, 064110 (2010).
- [17] See, e.g., L. Martin-Carron *et al.*, *Phys. Rev. B* **66**, 174303 (2002).
- [18] S. Chauhan, M. Kumar, and P. Pal, *RSC Adv.* **6**, 68028 (2016).
- [19] S. Goswami and D. Bhattacharya, *J. Alloys Compd.* **738**, 277 (2018).
- [20] See, e.g., S.M. Feng *et al.*, *New J. Phys.* **12**, 073006 (2010).
- [21] U. Chowdhury, S. Goswami, D. Bhattacharya, A.K. Midya, and P. Mandal, *Appl. Phys. Lett.* **109**, 092902 (2016).
- [22] J.T. Heron *et al.*, *Nature (London)* **370**, 516 (2014).
- [23] S. Goswami *et al.*, *Appl. Phys. Lett.* **99**, 073106 (2011); S. Goswami *et al.*, *Phys. Rev. B* **90**, 104402 (2014).
- [24] Z. Qiao, S.A. Yang, W. Feng, W.-K. Tse, J. Ding, Y. Yao, J. Wang, and Q. Niu, *Phys. Rev. B* **82**, 161414 (2010).
- [25] See, for example, X. Liu, C.Z. Wang, Y.X. Yao, W.C. Lu, M. Hupalo, M.C. Tringides, and K.H. Ho, *Phys. Rev. B* **83**, 235411 (2011).
- [26] Y. Labaye, O. Crisan, L. Berger, J.M. Greneche, and J.M.D. Coey, *J. Appl. Phys.* **91**, 8715 (2002).
- [27] J. Gou, X. Liu, K. Wu, Y. Wang, S. Hu, H. Zhao, A. Xiao, T. Ma, and M. Yan, *Appl. Phys. Lett.* **109**, 082404 (2016).